Experimental and theoretical comparison of spatially resolved laser-induced incandescence (LII) signals of soot in backward and right-angle configuration

Bladh, Henrik; Bengtsson, Per-Erik; Delhay, J; Bouvier, Y; Therssen, E; Desgroux, P

Published in:
Applied Physics B

DOI:
10.1007/s00340-006-2197-y

2006

Experimental and theoretical comparison of spatially resolved laser-induced incandescence (LII) signals of soot in backward and right-angle configuration

Henrik Bladh[1], Per-Erik Bengtsson[2], Jérôme Delhay[3], Yoann Bouvier[4], Eric Therssen[5], Pascale Desgroux[6]

1 Division of Combustion Physics, Lund Institute of Technology,
P.O. Box 118, SE-221 00 Lund, SWEDEN
Telephone: +46 46 222 03 53
Telefax: +46 46 222 45 42
Mail: henrik.bladh@forbrf.lth.se (*Corresponding author*)

2 Division of Combustion Physics, Lund Institute of Technology,
P.O. Box 118, SE-221 00 Lund, SWEDEN
Telephone: +46 46 222 31 09
Telefax: +46 46 222 45 42
Mail: per-erik.bengtsson@forbrf.lth.se

3 Physico-Chimie des Processus de Combustion et de l'Atmosphère
(PC2A, UMR CNRS 8522)
Centre d'Etudes et de Recherches Lasers et Applications
Université des Sciences et Technologies de Lille
59655 Villeneuve d'Ascq Cedex, France
Telephone: +33 3 20 43 49 31
Telefax: +33 3 20 43 69 77
Mail: jerome.delhay@ed.univ-lille1.fr

4 Physico-Chimie des Processus de Combustion et de l'Atmosphère
(PC2A, UMR CNRS 8522)
Centre d'Etudes et de Recherches Lasers et Applications
Université des Sciences et Technologies de Lille
59655 Villeneuve d'Ascq Cedex, France
Telephone: +33 3 20 43 49 31
Telefax: +33 3 20 43 69 77
Mail: Y.Bouvier@ed.univ-lille1.fr

5 Physico-Chimie des Processus de Combustion et de l'Atmosphère
(PC2A, UMR CNRS 8522)
Centre d'Etudes et de Recherches Lasers et Applications
Université des Sciences et Technologies de Lille
59655 Villeneuve d'Ascq Cedex, France
Telephone: +33 3 20 33 64 67
Telefax: +33 3 20 43 69 77
Mail: eric.therssen@univ-lille1.fr

6 Physico-Chimie des Processus de Combustion et de l'Atmosphère
(PC2A, UMR CNRS 8522)
Centre d'Etudes et de Recherches Lasers et Applications
Université des Sciences et Technologies de Lille
59655 Villeneuve d'Ascq Cedex, France
Telephone: +33 3 20 43 49 30
Telefax: +33 3 20 43 69 77
Mail: Pascale.Desgroux@univ-lille1.fr

Short title (max 120 characters): **Experimental and theoretical comparison of LII signals in backward and right-angle configuration**

PACS: *42.62.Fi, 44.40.+a*

Abstract

In-situ measurements of soot volume fraction in the exhausts of jet engines can be carried out using the laser-induced incandescence (LII) technique in backward configuration, in which the signal is detected in the opposite direction of the laser beam propagation. In order to improve backward LII for quantitative measurements, we have in this work made a detailed experimental and theoretical investigation in which backward LII has been compared with the more commonly used right-angle LII technique. Both configurations were used in simultaneous visualization experiments at various pulse energies and gate timings in a stabilized methane diffusion flame. The spatial near-Gaussian laser energy distribution was monitored on-line as well as the time-resolved LII signal. A heat and mass transfer model for soot particles exposed to laser radiation was used to theoretically predict both the temporal and spatial LII signals. Comparison between experimental and theoretical LII signals indicates similar general behaviour, for example the broadening of the spatial LII distribution and the hole-burning effect at centre of the beam due to sublimation for increasing laser pulse energies. However, our comparison also indicates that the current heat and mass transfer model overpredicts signal intensities at higher fluence, and possible reasons for this behaviour are discussed.

1. Introduction

One of the major pollutants from combustion processes is soot, and both the health aspects [1,2] and impact on the environment at large makes it important to reduce these emissions. Soot formation is a result of incomplete combustion, which is a sign of non-optimal efficiency of the process. The overall reduction of carbon dioxide emissions in the atmosphere that is needed in order to meet the legislative actions against the green-house effect puts great demands on improving the efficiency of combustion devices. Recently the soot emissions themselves have been discussed with regards to their direct and indirect role in global warming [3-5].

In-situ monitoring of pollutants is a powerful tool in the development of more efficient and clean combustion devices. One of the most promising techniques for *in-situ* measurements of soot volume fractions is laser-induced incandescence (LII), see [6] and references therein. In this technique soot particles are exposed to a rapid nano-scale laser pulse that heats the particles to their sublimation temperature. The increased thermal emission from the particles can readily be detected using photomultiplier tubes (for time-resolved detection) or CCD cameras (for spatially-resolved detection, i.e. imaging). The relation between the LII signal and the soot volume fraction has been investigated in many studies. Melton [7] showed theoretically that the prompt LII signal was proportional to D^x where $x = 3+0.154/\lambda_{det}$ (D = particle diameter, λ_{det} = detection wavelength in μm). For detection wavelengths in the visible spectral range it means roughly a proportionality between LII signal and soot volume fraction. This proportionality has also been experimentally verified in well-characterized flames by comparing LII with other techniques, mainly based on extinction [8-10].

The LII signal is an isotropic signal and can be detected along any angle. Detection is, however, usually set up in a right-angle configuration. This means that the signal is detected at a 90-degree angle (right-angle) with respect to the incident laser beam. This configuration has the advantage of enabling good spatial resolution in all three dimensions including the laser beam propagation direction. Right-angle and near right-angle LII has been used also for aircraft emission measurements [11] but due to

the harsh environment near these devices these configurations are not ideal. Detection of the LII signal in the opposite direction of the propagation of the incident laser beam (backward LII) has turned out to be a promising alternative in this respect [12], since it simplifies the experimental setup considerably making it possible to mount both laser and detector system inside one shielded box located at a safe distance from the engine [13]. The most obvious disadvantage with the backward configuration is that the measurements will be averaged along the laser beam (i.e. line-of-sight averaging). However, if a reliable quantification of the data can be achieved, quantitative average soot volume fractions can be obtained online during engine test runs.

The quantification remains one of the most critical issues with the LII technique regardless of configuration and a calibration method is needed. Experimentally this has been done for instance using extinction-based techniques in flat calibration flames (see for example Bengtsson *et al.* [10]). The sensitivity of this technique can be further enhanced by using a cavity ringdown setup [14,15]. Another solution for calibration is to use a two-colour LII approach in combination with a calibration lamp [16,17].

Even if the LII technique can be readily used, a lot of its aspects are partly unknown. One typical result of this is the different shapes obtained on so-called fluence curves, i.e. the LII signal intensity as function of laser fluence. In the low-fluence regime, the particle temperature increases strongly for increasing laser fluence and consequently the LII signal increases strongly as well. At moderate fluences, for 1064 nm excitation ~0.1 J/cm^2, the sublimation temperature of soot is reached, and instead of the strong increase in temperature, matter from the particles will sublime into gaseous species of partly unknown composition [18]. This mass reduction reduces the volume of soot and hence also the LII signal. Another additional complexity is that most laser beams have a non-uniform spatial distribution of energy, meaning that the low-fluence regime and higher fluence regimes coexist within the measurement volume making interpretation more difficult [19].

Theoretical models of the LII signal dependence on experimental parameters (laser pulse, detection characteristics) and theoretical parameters (soot properties, gas properties) have been developed and applied for more than 20 years [7,20-26].

However, there are uncertainties in the physical and chemical processes in the interaction between laser radiation and soot particles, as well as in the material properties of soot and gaseous species in the flame. Results giving improved knowledge in these areas thus lead to continuous improvement of the LII models. The basic principle of an LII model is that heat and mass balance equations are solved as function of time for one soot particle of a certain size. The time-resolved signal response from the particle can be calculated and subsequently the signal response from a measurement volume can be predicted theoretically. Traditionally only the processes absorption of laser pulse energy, heat transfer to surrounding gas, sublimation, and thermal radiation were part of the LII model, but recently additional effects such as thermal annealing, photofragmentation and oxidation have been considered [25].

To improve LII as a quantitative tool for extraction of soot properties, the models describing the heat and mass transfer between the particles and the surrounding gas must be tested against well-characterized experiments. In previous studies such efforts have mainly been performed on time-resolved data obtained from single point measurements, see for example [27-29]. In this work, one of the aims is to investigate backward LII and compare it to the more well-known right-angle setup. Hence studies were made using gated ICCD cameras, in which the measurement volume within a methane diffusion flame were imaged (in two dimensions) for these two different angles simultaneously. An LII model was applied for predicting the signal response from a fine mesh of points within the measurement volume, hence making it possible to create modelled signal images corresponding to the ones obtained experimentally. Comparison is made between these images and conclusions are drawn with respect to the theoretical model. Time-resolved measurements are also presented and compared to model results.

2. Experimental setup

The piloted jet burner consists of a hybrid McKenna burner (manufactured by Holthuis Inc.) equipped with a central stainless-steel injector of 4 mm-inner diameter, and is shown in Fig. 1. The results presented in this work are obtained in a sooting laminar (Re = 34) methane diffusion flame (Q = 100 cm^3/min., v = 13.7 cm/s). Measurements were performed 35 mm above the injector in a flame zone presenting a axi-symmetric soot distribution. At this height, the soot volume fraction, as checked by LII measurements, was found constant over a height of several millimetres. The surrounding premixed flat flame of methane and air (v = 12 cm/s) serves to stabilise the diffusion jet flame. Perturbations from ambient air were minimized by a shielding air flow (v = 73 cm/s). A quartz collector located 50 mm above the flat flame burner also improved the flame stability.

The experimental set-up is shown in Fig. 2. The laser is a Nd:YAG laser (Quantel Brilliant) operating at 1064 nm. Using a 1-mm diaphragm, the central part of the unfocussed near-Gaussian laser beam was selected and the beam propagated through the flame in the horizontal direction. The energy after the diaphragm was varied between 0.01 mJ and 8 mJ using the combination of a half-wave plate and a Glan prism.

The characteristics of the laser beam in terms of spatial energy distribution were monitored using a CCD-camera (Gentec EO WinCamD). The faint laser beam reflection created by the entrance surface of the dichroic mirror was, after a second reflection on a glass plate, aligned through a series of neutral density (ND) filters onto the chip of the CCD-camera. The distance from the CCD camera to the diaphragm was the same as from the flame to the diaphragm. A spatial resolution of 9.4 microns was obtained in both the horizontal and vertical dimension of the chip. Fig. 3 displays the spatial distribution of the laser beam energy for a pulse energy of 2.0 mJ (corresponding to a fluence of 0.14 J/cm^2). The spatial laser energy profile was recorded for all pulse energies used during the LII measurements. Analysis showed that it was almost independent of pulse energy.

The sooting region of interest was imaged using two directions of observation: one perpendicular to the laser propagation direction (right-angle LII) leading to images of the spatial LII distribution averaged across the beam, and the other one opposite to the propagation direction of the incident laser (backward LII) leading to images of the spatial LII distribution averaged along the laser beam. The two configurations are illustrated in Fig. 4 together with examples of 2D-images, and a coordinate system that will be useful for the orientation of the images in the figures presented later.

In the backward LII configuration, incandescence was collected backwards within a solid angle of about $2.1 \cdot 10^{-5}$ steradians. The LII signal was reflected by a 10-cm diameter dichroic beam splitter, spectrally filtered between 400 and 700 nm and imaged on a 1280x1024 pixels ICCD Dicam Pro camera (pixel size = 6.7 μm) using a 94 mm UV CERCO camera lens. The magnification was set to 13, thus one pixel in the image corresponds to 87.5 μm in the flame. A typical backward LII image has been inserted in Fig. 4. With right-angle LII, the broadband LII signal was collected perpendicular to the laser propagation direction using a set of two doublets (f_1 = 400 mm and f_2 = 200 mm) and imaged onto a ICCD Princeton camera with 384x576 pixels (pixel size = 22 μm). For this camera one pixel in the image corresponds to 44 μm in the flame. A typical right-angle image has also been inserted in Fig. 4.

The whole incandescent volume was imaged on a horizontal slit placed in front of a head-on photomultiplier tube (PMT), Philips XP2020Q (1.5-ns rise-time), for time-resolved LII measurements. The LII signal was spectrally filtered using a RG 630 filter leading to transmission in the region 630-900 nm. The PMT signal was digitized and stored by an oscilloscope (Tektronix, TDS 654 C, 500 MHz bandwidth, 4 GS/s sampling rate).

3. Theoretical approach

In an ideal situation, in which the physical conditions within a measurement volume can be assumed to be homogeneous, the spatial distribution of the LII signal would only be expected to change as function of local laser fluence within this volume. Thus the LII signal distribution can theoretically be calculated using a model for the signal response obtained from one soot particle exposed to a laser pulse with known

properties, together with knowledge of the spatial distribution of laser energy, i.e. the local fluence (J/cm^2).

The heat and mass transfer model used to predict the LII signal response is based on the one originally presented by Melton [7], and is described in detail elsewhere [26]. It consists of one heat and one mass balance equation which are both dependent on the particle temperature and the particle diameter. The coupled differential equations are solved numerically. With both temperature and diameter known as function of time, the LII signal can be modelled in a second step integrating the predicted signal over the detected wavelength region. In this work some of the physical parameters of the model presented in [26] have been updated. The constant values previously used for a number of parameters, including heat capacity c_s and density ρ_s of soot as well as the heat transfer coefficient k_a and the heat capacity C_p of the surrounding gas have been replaced by temperature-dependent functions [25]. The thermal accommodation coefficient α_T is set to 0.3 [25] and the absorption function $E(m) = \mathrm{Im}((m^2-1)/(m^2+2))$ to 0.296, a value obtained by using the dispersion relation by Dalzell and Sarofim at a wavelength of 1064 nm [30]. The parameter m is the complex refractive index of soot. The absorption function must also be used for calculating the LII signal, and since broad-band detection was used, the wavelength-dependence of the $E(m)$ is required. Since it is generally believed that the $E(m)$ varies very little with wavelength in the visible region (See for example [31]), the parameter was treated as constant in this work, and as a constant the relative shape of the calculated signal is unaffected by the exact choice of $E(m)$. For simplicity the $E(m)$ was set to 0.296 also when evaluating the signal response.

The experimental investigations have been performed using two-dimensional imaging in both right-angle and backward LII configuration, as well as time-resolved detection. Theoretical predictions of these signals can be obtained using the scheme presented in Fig. 5. A three-dimensional mesh of points is created covering the entire measurement volume, and the location of this mesh is depicted in Fig. 4. In every point (cell) the laser fluence and the soot volume fraction was defined. The laser fluence was directly calculated from the laser energy, the spatial laser energy profile, and the mesh resolution, which was 9.4 microns along x and z, and 35 microns in the

y-dimension. The soot volume fraction profile spatially resolved along the y-axis through the flame was measured using right-angle LII and that data was given as input for the heat and mass transfer model. The particle size distribution was assumed to be monodisperse and homogeneous throughout the volume. Flame temperature was also considered homogeneous and a value of 1800 K was used.

The heat and mass transfer model was used to predict the LII signal from each cell in the mesh. Broadband detection was used for both gated and time-resolved measurements, and to model the signals, filter functions defining the wavelength-dependent sensitivity were created for each detector system based on the optics, filters and specifications of each system. For creation of images, the time-resolved signal curve was numerically integrated with the same gate timing as used during the experiments. The calculations resulted in a tensor of intensity values – one from each cell in the three-dimensional measurement volume. Assuming a depth of field much larger than the measurement volume and perfect imaging, the resulting backward and right-angle LII images can be created by adding the pixel information along one of the tensor dimensions. By imaging target grids at different positions, the assumption was found to be valid for the depth of field, and therefore all parts of the measurement volume could be considered as being in focus. However, the spatial resolution was found to be drastically decreased by both imaging systems compared to the resolution of the model grid, which was given by the resolution of the beam-profile CCD camera. Therefore a routine was created in order to filter the model data to create output images with the same spatial resolution as the experimental ones. The routine essentially consists of a convolution with a Gaussian 2D function of certain width to simulate non-perfect imaging, and at the end also pixel binning that accounts for the difference between the mesh resolution and the pixel size of the two cameras. The input parameters were determined empirically using the target grid measurements individually for each camera system, among which the backward LII system had the lowest spatial resolution.

The time-resolved data recorded by the PMT was theoretically modelled using a weighted sum of all time-resolved signal curves obtained from the model over the fluence span investigated. As for the images, weighting coefficients were determined using the fluence data from the beam-profile CCD camera. A histogram was created

from each fluence profile image where the number of pixels within the image having the same fluence value could be readily extracted. The histogram information was used to weight the linear-combination of time-resolved LII signal data obtained from the heat and mass transfer model thus creating the overall time-resolved signal from the measurement volume.

This approach is based on several assumptions, some of which will be addressed in the discussion of the results. First of all it is assumed that the temporal distribution of laser energy is constant within the whole measurement volume and that only the local fluence changes spatially. The model hence uses the same temporal distribution of laser energy for all parts of the volume. Lacking on-line monitoring of the temporal distribution, a Gaussian distribution with the full width at half maximum specified by the laser manufacturer was used. Another assumption is that the effects of absorption on the signal are negligible. A laser beam that penetrates a region of soot will be absorbed along the path, effectively decreasing the local laser fluence as function of penetration depth. Yet another effect of absorption is self-absorption of the signal as the LII radiation originally created by the soot particles partly is absorbed by other soot particles in the cross-region between the measurement volume and the detector. The peak soot volume fraction in the methane flame was obtained from soot extinction calibration by Cavity Ring-Down Spectroscopy and found to be 350 ppb at 35 mm above the burner [32], which means that the absorption would be ~1% in this case. Finally the properties of the soot and the flame are assumed to be constant within the measurement volume. Thus the primary particle diameter, the flame temperature, and the refractive index are assumed to have the same values throughout the volume.

4. Results and discussion

4.1 Spatially resolved LII signals

Two-dimensional images of spatial LII signal distributions are presented in Fig. 6 for both the backward LII and right-angle LII configuration. Both theoretical and experimental images are shown for a choice of four different fluences. Since the

results in this work are obtained from an inhomogeneous spatial distribution of laser energy, the presented material, if not stated otherwise, is given as function of mean fluence, here defined as the laser pulse energy divided by the cross section of the beam profile at the $1/e^2$ intensity level. The first case at low fluence (0.07 J/cm^2) is clearly below the sublimation threshold whereas the images at 0.28 J/cm^2 and above show signs of reduced signal at the centre of the beam due to sublimation. For the experimental data, the inverted greyscale intensity is proportional to the signal intensity registered by each camera after background subtraction, and for the model data the inverted greyscale intensity is proportional to the irradiance from the individual mesh cells of the measurement volume tensor. The images have been auto-scaled to the maximum value within one column facilitating direct comparison of the intensity between the images of different laser fluences for a certain configuration. The backward LII images give the LII signal spatially integrated along the y-axis (approximately 10 mm) as shown in Fig. 4. The right-angle LII images are spatially integrated along the 90-degree angle i.e. in the x-direction (approximately 1 mm). The data sets have been obtained using a prompt LII signal (delay = 0) and a gate width of 100 ns. Throughout this paper we use the definition of the delay time zero as the moment when the laser pulse starts.

When observing the images in Fig. 6 it can be seen that the general agreement between model and experiment is good. It is clearly shown that (1) the spatial laser energy distribution widens for increasing energies and (2) a hole is formed at the centre of the beam. This hole-burning effect is obvious in both the images from backward LII and right-angle LII at 0.56 J/cm^2 and is a result of the high degree of sublimation in these regions [19]. When comparing with the theoretical calculations at the same fluence, the hole-burning effect is more evident in the backward LII image than in the right-angle LII image. Images like the ones in Fig. 6 are used for the graphs presented in the forthcoming Figs 7 and 8.

In Fig. 7, the experimental and theoretical cross sections have been plotted for backward LII and right-angle LII for various laser fluences. In this representation of the data the spatial widening of the LII signal distribution and the hole-burning effect for increasing fluence is even more evident. In addition it can be observed that the maximum signal decreases at high laser fluences. Mainly this is believed to be a result

from reduced spatial resolution in the images due to the imaging system of the detectors, and the modelled data have been compensated for this resolution reduction using the previously described scheme with the spatial filter. The main discrepancy between the experimental data and the theoretical calculations is that the hole-burning effect is much more pronounced in the experimental data.

The gate timing used for the results in Figs 6 and 7 is 100 ns and since detection is prompt, both the LII signal during the laser pulse duration and part of the decay is captured. Competing processes are governing the appearance of the signal at these different time domains, thus justifying a comparison of the signal obtained with a shorter gate and different delay timings. In Fig. 8 the cross sections through the backward LII signal as function of delay time is shown for three laser fluences. Cross sections from modelled images are also shown for comparison. For the lowest fluence at 0.07 J/cm^2 the cross section seems reasonably well predicted by the model. The fluence is not high enough to result in sublimation and the "bell shape" is apparent for all profiles. A normalized plot with the same data (inserted) also reveals that the shapes of the profiles are nearly identical. The choice of model and parameters for the particle emissivity has a great impact in this regime, and this will be further discussed in subsection 4.4. For the fluence at 0.25 J/cm^2, a plateau is apparent in both the experimental and theoretical data for the delayed gates, while the prompt gate remains bell-shaped. Clearly we see the influence of sublimation in the central regions of the measurement volume, at this moderate fluence only visible for the delayed gates. For 0.56 J/cm^2, a substantial decrease of signal at the centre of the beam is obtained. Similar to the case of the 100 ns gate of Figs 6 and 7, the decrease is underpredicted by the model. This comparison also highlights another discrepancy. The signs of sublimation seem to appear earlier in the experiments than predicted by the model. This is evident when comparing the signals for the prompt gate (delay time 0 ns) for 0.56 J/cm^2 where the experimental data clearly shows a decrease of signal at the centre of the beam, whereas the cross section through the theoretical signal, though broadened as compared to the same signal at lower energies, remains bell shaped.

The presented results in Figs 6-8 suggest that a kinetically controlled sublimation process used in the present model may be insufficient to explain the total mass loss mechanism present during the LII process. Since the kinetically controlled

sublimation mechanism is initiated first when the particle temperature approaches ~3915 K [18], signal decrease will not be predicted to take place until several nanoseconds after the start of the laser pulse. For instance, at the highest peak fluence (~1 J/cm^2) at the very centre of the beam in the images at 0.56 J/cm^2 (Fig. 8), the model predicts particle mass loss to start approximately 10 ns after the start of the laser pulse. Images recorded with a 20 ns prompt gate will thus not be influenced by the signal decrease due to mass reduction to the same degree as the delayed gates. Recent results by Yoder *et al*. [33] obtained using combined LII and Rayleigh scattering indicate that the mass loss in reality occurs much earlier. At a fluence of 0.61 J/cm^2 in their work, mass loss and laser heating was found to occur on the same time-scale. Since particle temperatures could not have reached temperatures close to the sublimation temperature of soot at these early times, a non-thermal laser ablation process was suggested [33]. A possible physical process with these characteristics has been proposed by Michelsen [25]. The process, referred to as non-thermal photodesorption, predicts mass loss due to photo-ablation. The laser pulse electronically excites surface states of the particles which results in photo-ablation of C, C_2 and C_3.

The inclusion of a mass loss mechanism initiated earlier than the kinetically controlled sublimation mechanism is assumed to decrease not only the delayed LII signal, but also the absolute intensity of the prompt signal. Some support for this is presented by Michelsen [25], who predicts a plateau regime in the maximum intensity of modelled time-resolved LII signals as function of laser fluence when including a non-thermal photodesorption term in the model, a feature also obtained in experiments using a near-tophat profile [25]. The model used in this work predicts instead of a plateau, a steady increasing maximum signal with fluence (see ref. [26]), and resembles the original Melton model in this respect. The predicted decrease in particle diameter and the time at which the process is initiated is not the only factor affecting the predicted signal decrease at high fluences. Also the maximum particle temperature is important. The temperature is strongly fluence-dependent in the low-fluence regime, but as the temperature approaches the sublimation temperature, the fluence-dependence decreases. Studies of the maximum particle temperature as function of laser fluence have shown somewhat different behaviour regarding the fluence-dependence. Schraml et al. used a scheme in which a large portion of the

spectrum was detected using a spectrometer and fast CCD camera [34]. The authors found increasing maximum soot temperatures in the fluence range 0.5-2.5 J/cm^2 indicating that superheating of the particles occur. The model used in our work, predicts super-heating and thus particles reach soot temperatures substantially higher than 4000K for higher fluences. In a recent study by de Iuliis *et al.* [17] in which time-resolved data from PMTs are used for temperature evaluation, the maximum particle temperature reaches a constant value of around 4000 K at fluences above ~0.2 J/cm^2, which would indicate that no super-heating of the particles occurs. The different experimental results obtained may be explained by the difficulties involved in the task of accurately measure the maximum soot temperatures during LII for which both high spectral and temporal resolution is needed. In order to obtain a more complete understanding of the LII process and its dependence on laser fluence, further studies on both particle temperatures and sizes with high temporal resolution are needed.

4.2 Fluence dependence of LII signals

When creating experimental data sets to validate LII models, much effort has been put on accomplishing uniform spatial distribution of laser energy, i.e. a top-hat profile, using for instance relay imaging [17,25,28]. This would ensure that all particles reach the same maximum temperature and are experiencing the same degree of mass loss, making detected signals directly comparable with model results. Creating a near-perfect top-hat profile is sometimes, however, an extremely demanding task, and here the backward LII technique opens up an alternative approach. For backward LII the averaging is essentially made along the laser beam axis, and assuming absorption to be negligible, the signal in a certain region within the backward LII image should be originating from a region with nearly homogeneous fluence. In this work the spatial distribution of laser energy is well characterized and found to be near-Gaussian. Using the signal contribution from the centre region of the measurement volume, where the fluence has its maximum and hence is relatively homogeneous, it should be possible to derive tophat fluence curves. The limited spatial resolution will, however, always introduce some spatial averaging, and therefore we choose not to refer to such data as real top-hat, but rather quasi-tophat.

In Fig. 9 such quasi-tophat curves are shown together with fluence curves derived from the total intensity in the images. In an attempt to avoid spatial averaging as much as possible the quasi-tophat curves have been created using only the centre pixel intensity from the backward LII signal data. In order to directly compare with results from the model, the same treatment was carried out on the theoretical images. The quasi-tophat data are presented as function of peak fluence, and the total signal as function of mean fluence. Two gate timings are shown, one prompt with 20 ns gate and one delayed with 100 ns gate. The curves have been normalized to the peak fluence 0.2 J/cm^2 (which corresponds to the mean fluence 0.11 J/cm^2) in order to facilitate comparison of the shapes, and it is emphasized here that no absolute intensity comparisons between model and experiment are intended. For both the quasi-tophat and total fluence curves it is apparent how the experimental and theoretical profiles of the 20 ns prompt gate deviate from each other much more than is the case for the same curves of the delayed gate. Though apparent in both data sets, it is more pronounced in the quasi-tophat comparison, where the theoretical prediction of the prompt 20 ns gate profile never stops increasing with energy, while its experimental counter-part decreases somewhat. Also this discrepancy may be explained by the inability of the current sublimation model to account for the signal decrease at higher fluences, and more specifically early during the laser pulse. Discrepancies are also apparent for the 100 ns delayed gate, even if they seem less pronounced. Another issue visualized in Fig. 9 is the shape of the quasi-tophat curves in the high fluence regime. The shape of the experimental curves differs quite substantially from those of the theoretical predictions. At the highest fluences the curve flattens out almost reaching a constant value, while the model predictions only show a slight tendency of levelling out at the same fluences. This issue has been discussed by Witze *et al.* [35] and in their data a plateau regime is obtained in the range 1-1.6 J/cm^2, i.e. just above the highest peak fluences used in this work.

4.3 Time-resolved LII signals

The time-resolved signals obtained during the experiments are as previously mentioned spatially averaged over different flame conditions and do not serve the purpose of direct model validation. In addition the spatial distribution of laser energy is inhomogeneous yielding averaging over a range of fluences. Since no previous data

on primary particle sizes in the diffusion flame was available, the main purpose of the time-resolved data was to determine a rough value on the primary particle size to use for the theoretical calculations presented elsewhere in this paper.

Following the scheme presented earlier for creation of the LII signal images, a weighted summation of time-resolved model results in a range of fluences was created. Since no filter was used in front of the PMT, the wavelength-dependent filter function that is used for the LII signal evaluation was determined by the detector efficiency and transmission characteristics of the focussing optics. Normalized time-resolved curves from experiment and weighted summations of modelled signals are shown in Fig. 10 for three different mean fluences. By regarding the primary particle size distribution as monodisperse in lack of better knowledge of the flame conditions, a best fit in least-square sense could be found for D = 13 nm. However, it was not possible to get good agreement between model and experiment at all recorded fluences, and as could be seen in Fig. 10, the high-fluence regime is better reproduced than the low-fluence regime for this choice of primary particle size. It might be argued that the low-fluence regime would be a better choice of data set for comparison with the model that we know has large uncertainties in the treatment of the high-fluence regime. However, with the methodology used, in which the primary particle diameter was treated as the only unknown variable, it was not possible to get good agreement among the low-fluence data set for one choice of the primary particle diameter, whereas it was achievable for the medium and high-fluence regime. This effect may be a result from errors in the current heat transfer term, or have its origin in the flame conditions, of which we do not know the size distributions and soot morphology. The effect may also be a result from a physical process not included in the present model, and indeed similar behaviour was found by Witze *et al.* in their low-fluence data [35]. In Ref. 35 it is suggested that thermal annealing may be an important process explaining these discrepancies, and later Michelsen has shown that the influence of the annealing term as implemented in her model is high also at lower fluences [25,28]. However, the uncertainties associated with the present data and flame conditions are too high for conclusions to be drawn about the influence on such effects on low-fluence LII.

4.4 Some parameters in the model and its implications

The results presented in the previous sections highlight one major issue, which is that the model seems to underestimate the signal decrease at high fluences. Before discussing completely new physical mechanisms, a discussion with regards to the parameters and functions within the current model could be undertaken. One natural starting point is the absorption function $E(m)$, which linearly scales the size of the absorption term in the model, and hence influences the whole signal appearance. One of the affected processes will inevitably be the mass loss. For high values of $E(m)$ predicted mass loss will be stronger for a given laser fluence. Following this statement, one could argue that a higher value on the absorption function should be used in the present comparison. The model results presented here are all based on the Rayleigh approximation for the emissivity, using a constant $E(m) = 0.296$, a value obtained from using the dispersion relation of Dalzell and Sarofim at 1064 nm [30]. The values readily available from literature at this wavelength range to the authors knowledge from around 0.20 to 0.42 [27,31]. Choosing 0.42 [27] instead of 0.296 would increase the absorption term with 42% and hence lead to higher degree of mass loss. However, the rise of the predicted fluence curve would also become steeper, and the fluence at which the signal has its maximum would decrease. This is shown in Fig. 11a for a 100 ns gate and a delay of 50 ns. Predicted quasi-tophat curves derived using three different literature values of $E(m)$ is shown together with the experimental curve. The general trends regarding the influence of $E(m)$ is the same for other gate timings.

Since it is reasonable to assume that the kinetically controlled mass loss mechanism is inadequate for predicting the real mass loss during the LII process, it could be of interest to discuss different parameters within the current model, and which influence they have on the overall signal. It is beyond the scope of this work to discuss the thermodynamical data currently used in the model. They have its origin in the equilibrium calculations from Leider *et al.* [18], and are implemented as polynomials given by Smallwood *et al.* [36]. However, the evaporation coefficient β, originally added by Kennard [37] in his derivation of the mass loss mechanism, is of interest for a small parameter study. Kennard derived the evaporation indirectly by utilizing the fact that evaporation and condensation occurs at equal rates when the vapour is

saturated. His expression for the evaporation is thus in reality a condensation term derived from kinetic gas theory, and the evaporation coefficient is added to take into account that not all molecules impinging on a surface will actually condense [37]. The value of the evaporation coefficient is unknown, but literature values are in the range 0.6-1.0 [38]. In Fig. 11b theoretical quasi-tophat fluence curves derived with three different values on the evaporation coefficient are compared to experimental results for the same gate timing as in 11a. It is clear from the comparison that the absolute signal will differ, at the same time as the shape of the curve remains relatively unchanged. Thus uncertainties in the exact value of the evaporation coefficient can not be responsible for the inability of the current mass loss mechanism in predicting the signal decrease at high fluences.

5. Summary

The backward-LII configuration is a practical solution for remote LII-measurements in harsh environments such as in aero-engine exhausts, and to develop it into a quantitative method the technique needs to be characterized. In this study, a detailed experimental and theoretical investigation has been performed on the backward laser-induced incandescence (LII) technique. It has been compared with the commonly used right-angle LII technique in simultaneous measurements where spatially resolved two-dimensional images have been recorded at different laser fluences and using different detection time gates. The measurements were made in a sooting methane diffusion flame with an approximate homogeneous soot volume fraction. A Nd:YAG laser wavelength of 1064 nm with a near-Gaussian beam profile was used for the excitation. Time-resolved LII signals were recorded simultaneously.

A theoretical model was developed, which included a heat and mass transfer model for single soot particles undergoing heating, cooling and mass reduction as a consequence of the interaction with the laser pulse, and it was applied to simulate the experimentally recorded LII signals. Theoretical and experimental two-dimensional images obtained from both the backward and right-angle LII configuration were in general in good agreement. The model was, however, found to underestimate the signal decrease for increasing laser fluences in the high-fluence regime. As a consequence this resulted in a stronger hole-burning in the centre of the experimental backward-LII images than predicted theoretically. Moreover, the results implicate that

the mass loss in reality occurs earlier than predicted by the current mass loss mechanism and we speculate that this might be due to a non-thermal process.

Acknowledgements

The authors would like to thank the European Commission for its financial contribution to this work within the AEROTEST project, contract N°AST3-CT-2004-502856, 6th PCRDT, Auxitrol S.A. and MECAPA (Pôle capteur, FRED, FEDER, Conseil Régional Centre). The CERLA (FR CNRS 2416) is supported by the French Research Ministry, by the Nord/Pas de Calais Region and by the European funds for Regional Economic Development. The authors thank the French Research Ministry under the contract D4P3 "Recherche Aéronautique sur le Supersonique". The work by the Swedish research group was also financially supported by the Swedish Research Council.

References

1. T.R. Barfknecht, Prog. Energy Combust. Sci. **9**, 199 (1983)
2. N. Künzli, R. Kaiser, S. Medina, M. Studnicka, O. Chanel, P. Filliger, M. Herry, F. Horak Jr., V. Puybonnieux-Texier, P. Quénel, J. Schneider, R. Seethaler, J-C. Vergnaud, H. Sommer, The Lancet **356**, 795 (2000)
3. M.Z. Jacobson, Nature **409**, 695 (2001)
4. S. Menon, J. Hansen, L. Nazarenko, Y. Luo, Science **297**, 2250 (2002)
5. J.E. Penner, D.H. Lister, D.J. Griggs, D.J. Dokken, M. McFarland (Eds.), *Aviation and the Global Atmosphere: A Special Report of the IPCC Working Groups I and III in collaboration with the Scientific Assessment Panel to the Montreal Protocol on Substances that Deplete the Ozone Layer* (Cambridge University Press, 1999).
6. R.J. Santoro, C.R. Shaddix: in *Applied Combustion Diagnostics*, ed. by K. Kohse-Köinghaus, J.B. Jeffries, (Taylor & Francis, London 2002) pp. 252-286
7. L.Y. Melton, Appl. Opt. **23**, 2201 (1984)
8. C.R. Shaddix, J. E. Harrington, and K. C. Smyth, Combust. Flame **99,** 723 (1994).
9. B. Quay, T. W. Lee, T. Ni, and R. J. Santoro: Combust. Flame **97**, 384 (1994)
10. P.-E. Bengtsson, M. Aldén, Appl. Phys. B **60**, 51 (1995)
11. T.P. Jenkins, J.L. Bartholomew, P.A. DeBarber, P. Yang, J.M. Seitzman, R.P. Howard, AIAA, paper 2002-3736, (2002)
12. J.D. Black, Laser-induced Incandescence Measurements of particles in Aero-Engine Exhausts, EOS/SPIE Meeting, Münich, June 14-18, Paper 3821-38 (1999)
13. K. Schäfer, J. Heland, D.H. Lister, C.W. Wilson, R.J. Howes, R.S Falk, E. Lindermeir, M. Birk, G. Wagner, P. Haschberger, M. Bernard, O. Legras, P. Wiesen, R. Kurtenbach, K.J. Brockkmann, V. Kriesche, M. Hilton, G. Bishop, R. Clarke, J. Workman, M. Caola, R. Geatches, R. Burrows, J.D. Black, P. Hervé, J. Vally, Appl. Opt. **39**, 441 (2000)
14. R.L. Vander Wal, Proc. Combust. Inst. **27**, 59 (1998)
15. C. Schoemaecker Moreau, E . Therssen, X. Mercier, J.F. Pauwels, P. Desgroux, Appl. Phys. B, **78**, 485 (2004)
16. D.R. Snelling, G.J. Smallwood, F. Liu, Ö.L. Gülder, W.D. Bachalo, Appl. Opt. **44**, 6773 (2005)
17. S. de Iuliis, F. Cignoli, G. Zizak, Appl. Opt. **44**, 7414, (2005)
18. H.R. Leider, O.H. Krikorian, D.A. Young, Carbon **11**, 555, 1973

19. J. Delhay , Y. Bouvier, E. Therssen, J. D. Black, P. Desgroux, Appl. Phys. B **81**, 181 (2005)
20. C.J. Dasch, Appl. Opt. **23**, 2209 (1984)
21. D.L. Hofeldt: SAE paper 930079 (Society of Automotive Engineers, Warrendale, PA 1993)
22. P. Roth, A.V. Filippov, J. Aerosol Sci. **27**, 95 (1996)
23. S. Will, S. Schraml, K. Bader, A. Leipertz, Appl. Opt., **37**, 5647 (1998)
24. D.R. Snelling, F. Liu, G.J. Smallwood, Ö.L. Gülder, 34th National Heat Transfer Conference, NHTC2000-12132 (2000)
25. H.A. Michelsen, J. Chem. Phys. 118, 7012 (2003)
26. H. Bladh, P.E. Bengtsson, Appl. Phys. B **78**, 241 (2004)
27. D.R. Snelling, F. Liu, G.J. Smallwood, Ö.L. Gülder, Combust. Flame, **136**, 180 (2004)
28. H.A. Michelsen, P.O. Witze, D. Kayes, S. Hochgreb, Appl. Opt. **42**, 5577 (2003)
29. S. Dankers, A. Leipertz, Appl. Opt. **43**, 3726 (2004)
30. W.H. Dalzell, A.F. Sarofim, J. Heat Transf. **91**, 100 (1969)
31. S.S. Krishnan, K.-C. Lin, G.M. Faeth, J. Heat Transf. **123**, 331 (2001)
32. Y. Bouvier, C. Mihesan, M. Ziskind, E. Therssen, C. Focsa, P. Desgroux, (submitted to the 31st International Symposium on Combustion)
33. G.D. Yoder, P.K. Diwakar, D.W. Hahn, Appl. Opt. **44**, 4211 (2005)
34. S. Schraml, S. Dankers, K. Bader, S. Will, A. Leipertz, Comb. Flame **120**, 439 (2000)
35. P.O. Witze, S. Hochgreb, D. Kayes, H.A. Michelsen, C.R. Shaddix, Appl. Opt. **40**, 2443 (2001)
36. G.J. Smallwood, D.R. Snelling, F. Liu, Ö.L. Gülder, J. Heat Transf. **123**, 814 (2001)
37. E.H. Kennard, *Kinetic theory of gases*, (McGraw-Hill, New York, 1938)
38. B.J. McCoy, C.Y. Cha, Chem. Eng. Sci. **29**, 381 (1974)

Figure Captions

Fig. 1. The experimental burner arrangement.

Fig. 2. Experimental setup. The burner is schematically represented (top view). PMT= Photomultiplier tube. L = Lens, f_1 = 400 mm and f_2 = 200 mm.

Fig. 3. The spatial energy distribution of the laser.

Fig. 4. The two studied LII configurations (backward LII and right-angle LII) and their relation to the measurement volume.

Fig. 5. The scheme for creation of modelled LII images directly comparable to experimental results.

Fig. 6. LII signal images obtained using both the backward and the right-angle configuration with a 100 ns prompt gate. Both experimental and theoretical data are shown for a choice of different mean fluences.

Fig. 7. Radial cross sections through both backward and right-angle LII signal images for a 100 ns prompt gate obtained from experiments (upper) and from theoretical model (lower). The profiles have been scaled to the maximum value among all profiles in each graph.

Fig. 8. Radial cross sections through the backward LII signal for different choice of delay time and a 20 ns gate. The profiles have been normalized to the maximum value within each plot, and the relative difference between the curves remains intact. The small inserts in the left column show the curve shapes being nearly identical when normalized.

Fig. 9. Fluence curves derived both from the total backward LII signal (lower figure) and the centre pixel of the same images (upper figure). Both experimental (solid lines) and theoretical (dashed lines) results are shown, and the corresponding curves for a certain choice of gate and delay have been normalized to the value at 0.2 J/cm^2 which corresponds to the mean fluence of 0.11 J/cm^2. Note that the relative signal strength between the curves from the experimental data has been left intact and the 20 ns gate multiplied a factor of 2.

Fig. 10. Modelled (solid lines) and experimental time-resolved signals for three laser fluences. The time-resolution of the data was 2 ns, but for better visualization all measurement points have not been included in the figure.

Fig. 11. Quasi-tophat fluence curves derived from the centre pixel of LII signal images for detection using a 100 ns gate delayed 50 ns. In a) results from modelled images is shown for three different values of $E(m)$. The value 0.296 is derived from

Dalzell and Sarofim [30] and is used in the present study, 0.366 comes from Krishnan *et al.* [31] and 0.42 from Snelling et al. [27]. All curves have been normalized to their maximum values. In b) results from modelled images are shown for three different values of the evaporation coefficient β. The experimental curve and the curve with β=0.8, which is used in the present work, have been normalized to their maximum values while the relative difference between the modelled curves have been left intact.

Figure 1

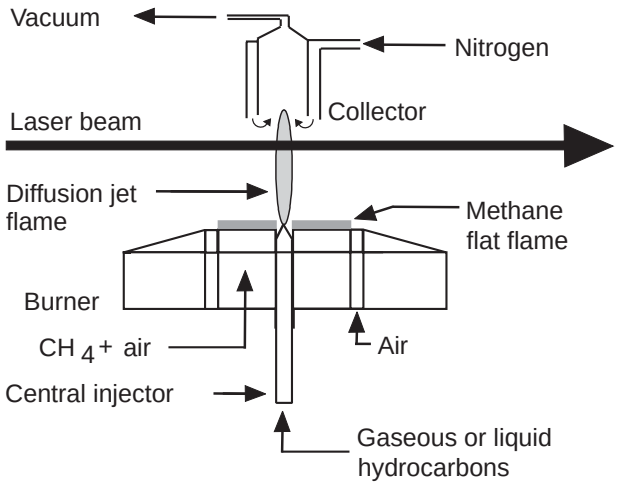
Vacuum
Nitrogen
Collector
Laser beam
Diffusion jet
flame
Methane
flat flame
Burner
CH 4 + air
Air
Central injector
Gaseous or liquid
hydrocarbons

Figure 2

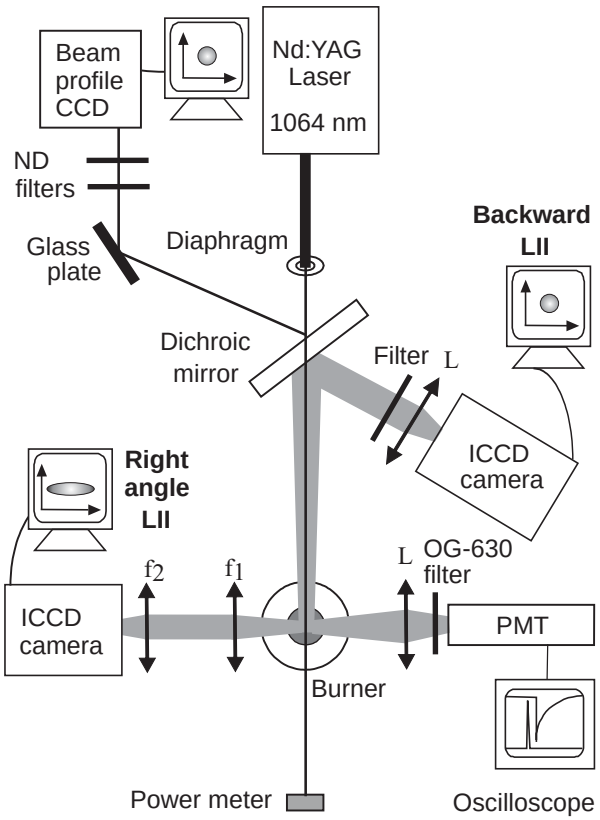
Beam profile CCD
Nd:YAG Laser
1064 nm
ND filters
Glass plate
Diaphragm
Backward LII
Dichroic mirror
Filter
L
ICCD camera
Right angle LII
f2
f1
L
OG-630 filter
ICCD camera
PMT
Burner
Power meter
Oscilloscope

Figure 3

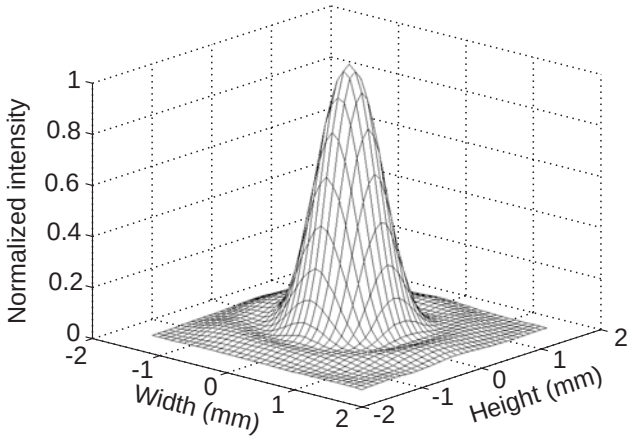
Normalized intensity
1
0.8
0.6
0.4
0.2
0
-2
-1
0
1
2
Width (mm)
-2
-1
0
1
2
Height (mm)

Figure 4

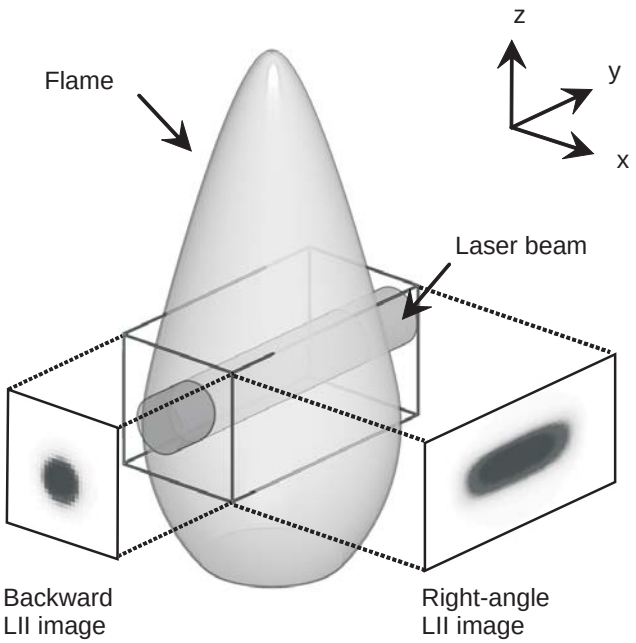
z
y
x
Flame
Laser beam
Backward
LII image
Right-angle
LII image

Figure 5

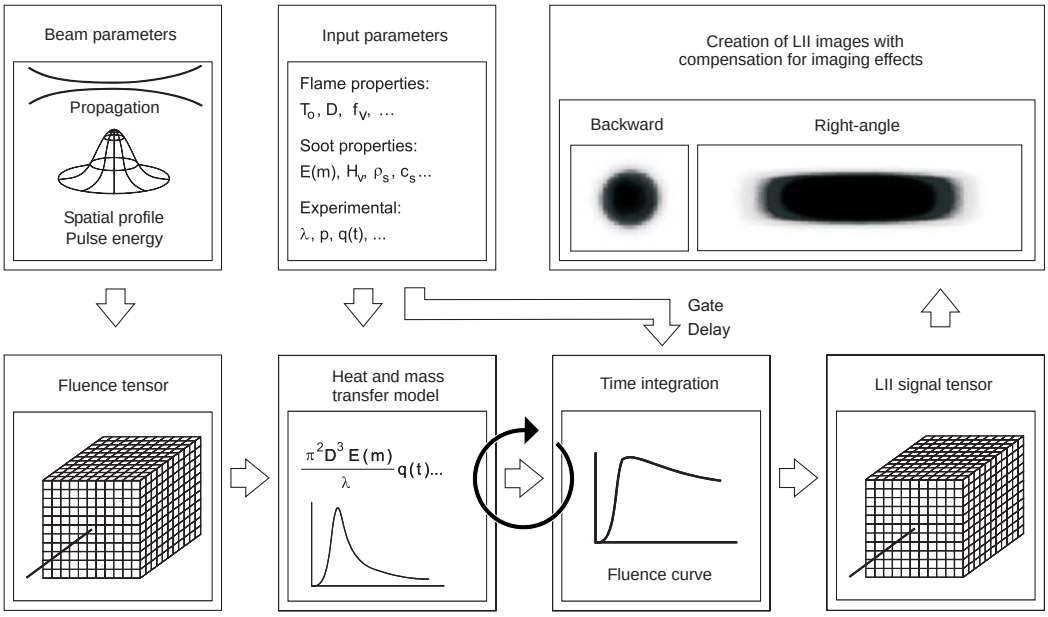
Beam parameters
Propagation
Spatial profile
Pulse energy
Input parameters
Flame properties:
T_o, D, f_V, …
Soot properties:
E(m), H_v, ρ_s, c_s…
Experimental:
λ, p, q(t), ...
Creation of LII images with compensation for imaging effects
Backward
Right-angle
Gate
Delay
Fluence tensor
Heat and mass transfer model
$\frac{\pi^2 D^3 E(m)}{\lambda} q(t)...$
Time integration
Fluence curve
LII signal tensor

Figure 6

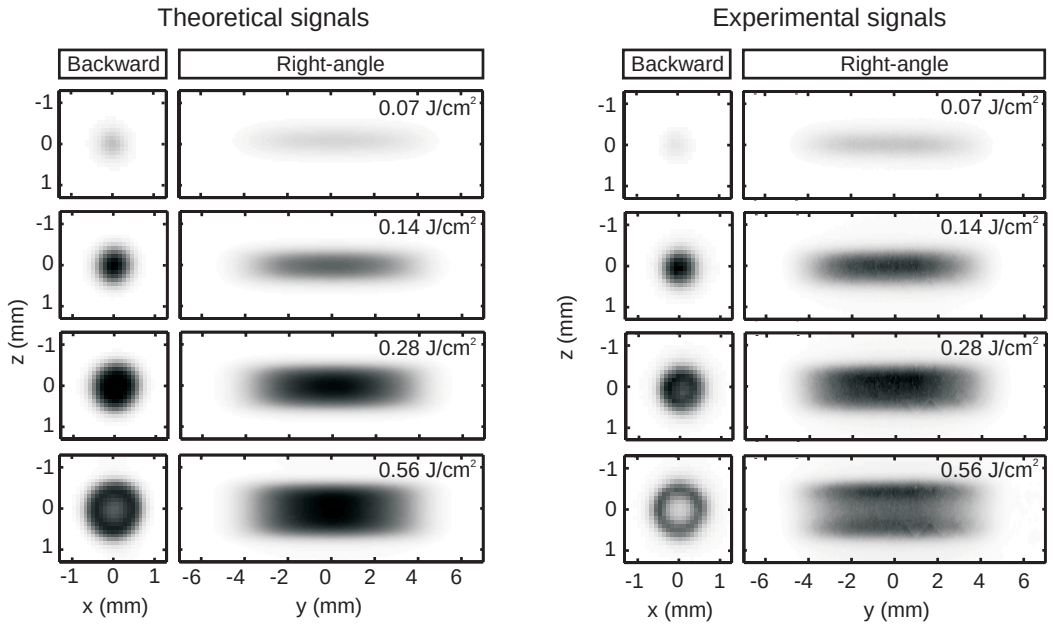
Theoretical signals
Experimental signals
Backward
Right-angle
0.07 J/cm²
0.14 J/cm²
0.28 J/cm²
0.56 J/cm²
z (mm)
x (mm)
y (mm)
-1
0
1
-6
-4
-2
2
4
6

Figure 7

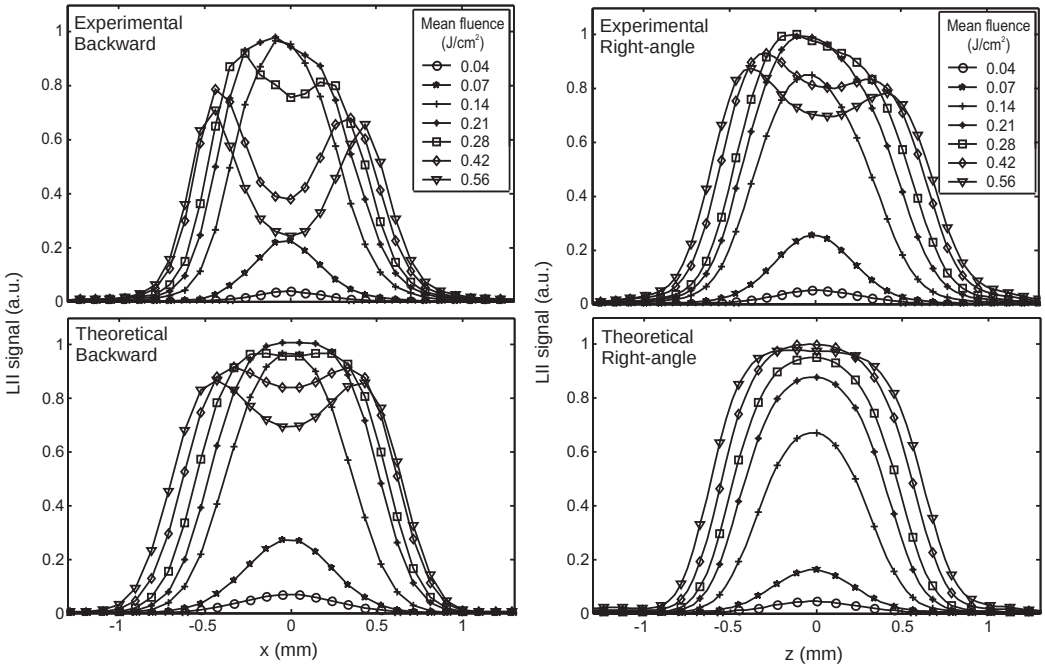
Experimental
Backward
Theoretical
Backward
Experimental
Right-angle
Theoretical
Right-angle
Mean fluence
(J/cm²)
0.04
0.07
0.14
0.21
0.28
0.42
0.56
LII signal (a.u.)
x (mm)
z (mm)

Figure 8

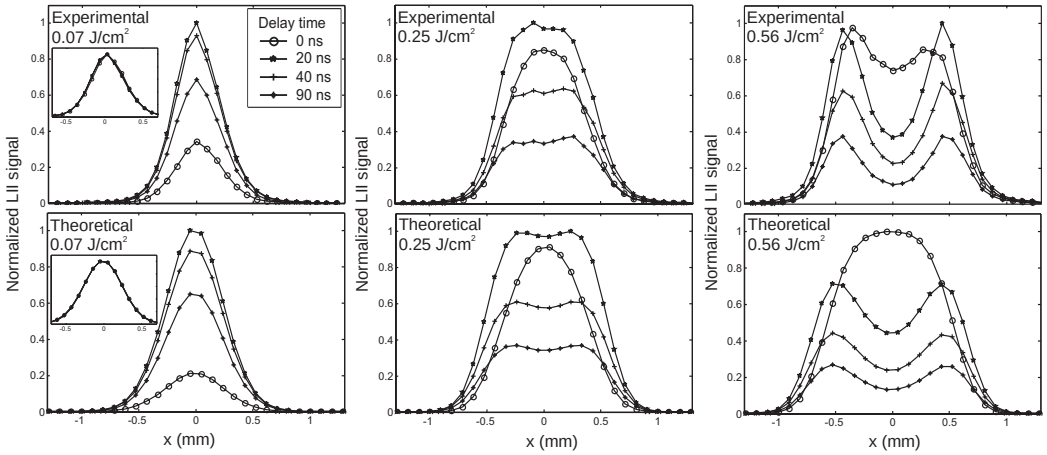
Experimental
0.07 J/cm2
Delay time
0 ns
20 ns
40 ns
90 ns
Theoretical
0.07 J/cm2
Experimental
0.25 J/cm2
Theoretical
0.25 J/cm2
Experimental
0.56 J/cm2
Theoretical
0.56 J/cm2
Normalized LII signal
x (mm)

Figure 9

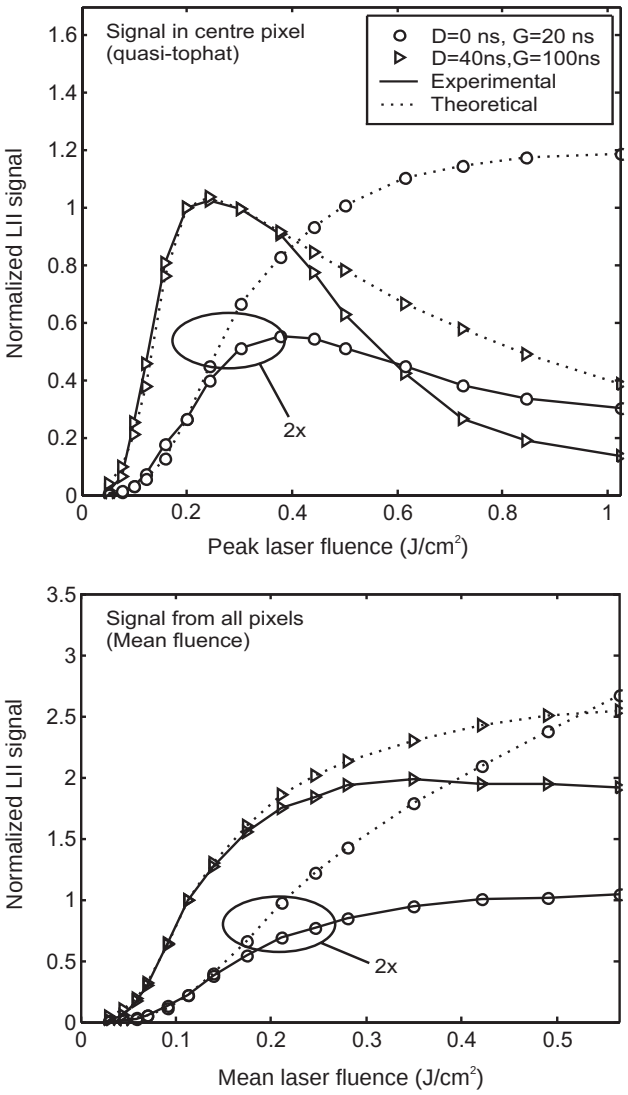
Signal in centre pixel
(quasi-tophat)
D=0 ns, G=20 ns
D=40ns,G=100ns
Experimental
Theoretical
Normalized LII signal
Peak laser fluence (J/cm²)
2x
Signal from all pixels
(Mean fluence)
Normalized LII signal
Mean laser fluence (J/cm²)
2x

Figure 10

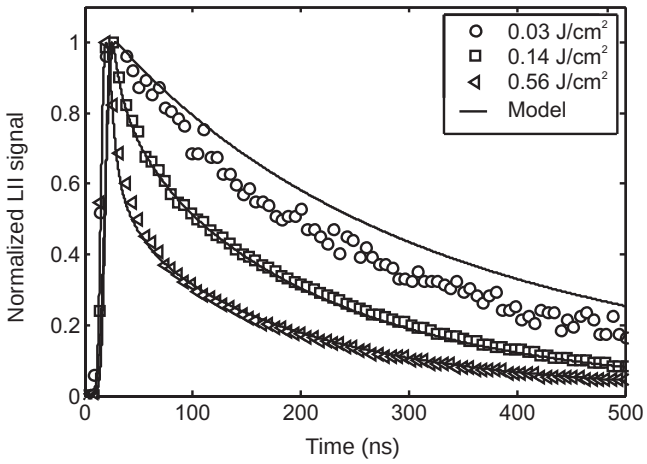
0.03 J/cm2
0.14 J/cm2
0.56 J/cm2
Model
Normalized LII signal
Time (ns)
0
0.2
0.4
0.6
0.8
1
0
100
200
300
400
500

Figure 11

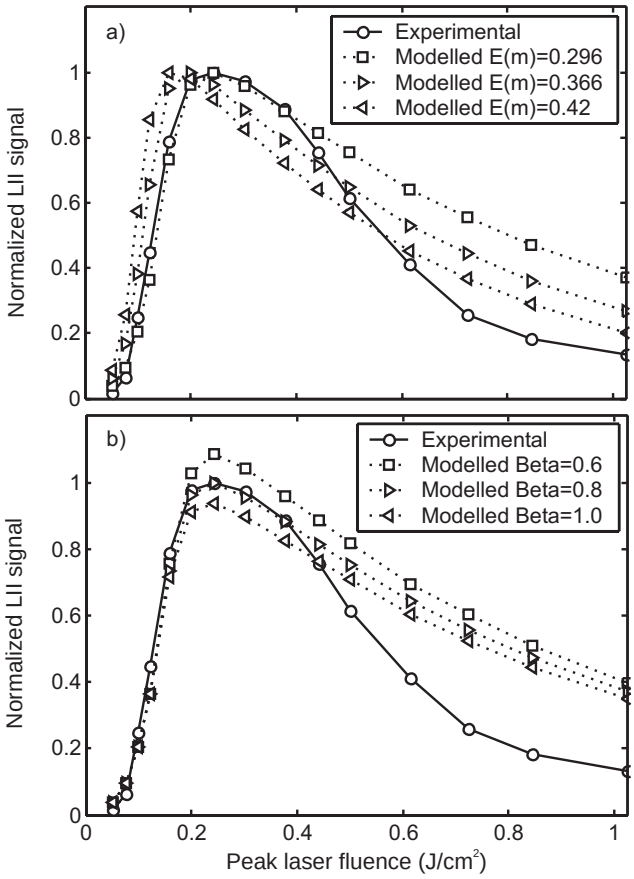
a)
Experimental
Modelled E(m)=0.296
Modelled E(m)=0.366
Modelled E(m)=0.42
Normalized LII signal
b)
Experimental
Modelled Beta=0.6
Modelled Beta=0.8
Modelled Beta=1.0
Normalized LII signal
Peak laser fluence (J/cm2)